SMALL-ANGLE NEUTRON SCATTERING AND BIOMOLECULES

by J. Katsaras, T.A. Harroun, J. Pencer, T. Abraham, N. Kučerka and M.-P. Nieh

Soft materials, both polymeric and biologically relevant, are rich in hydrogen. By coincidence, neutrons have the unique capability of scattering differently from hydrogen (coherent scattering length of hydrogen, $b_H = -0.37 \times 10^{-12}$ cm) compared to its isotope deuterium ($b_D = 0.67 \times 10^{-12}$ cm). As a result of this marked difference in scattering power (contrast) between native hydrogenated materials and their counterparts synthesized from deuterated monomer units, neutron scattering techniques have proven to be powerful tools for the study of soft condensed matter systems. Here, we will discuss the small-angle neutron scattering (SANS) technique, which is presently playing a pivotal role in extracting unique structural information from intrinsically disordered systems.

NEUTRONS

Neutrons are electrically neutral, subatomic, elementary particles, found in all atomic nuclei, except hydrogen (^{1}H). They are approximately 1,840 times more massive than an electron and have a nuclear spin of 1/2. Neutrons are only stable when bound by an atomic nucleus, while unstable free neutrons have a mean lifetime of approximately 900 s, decaying into a proton, an electron, and an antineutrino [1,2].

Because neutrons interact with atomic nuclei the scattering "power" (cross-section) of an atom is not strongly related to its atomic number. Neighbouring elements in the periodic table can therefore, have substantially different scattering cross sections [3]. More importantly, the interaction of a neutron with the nucleus of an atom allows neutrons to interact differentially with an element's isotopes. The classic example is the isotopic substitution of ^{1}H for deuterium (^{2}H) in polymeric materials [4,5]. As a result of their intrinsic properties, neutrons are used as follows:

(i)   Since they interact weakly with atomic nuclei, neutrons are highly penetrating. This feature allows neutrons to probe samples in complex sample environments, without the need to engineer neutron "windows" or ports into the sample enclosure. This enables the measurement of bulk processes under realistic conditions [6-8].

(ii)   Because the scattering ability of an atom is not strongly related to its atomic number, neutrons are used extensively to locate "light", low atomic number atoms among

> As a result of a marked difference in scattering power (contrast) between native hydrogenated materials and their counterparts synthesized from deuterated monomer units, neutron scattering techniques have proven to be powerful tools for the study of soft condensed matter systems.

"heavy" atoms. In the case of polymeric materials, neutrons are used to precisely locate hydrogen atoms [9,10].

(iii) ^{1}H has a negative scattering length giving it "contrast" when surrounded by other, positive scattering length atoms. For biological samples intrinsically rich in hydrogen, judicious substitution of ^{2}H for ^{1}H provides a powerful method for selectively tuning the contrast of a given macromolecule. By doing so, one can accentuate, or nullify, the scattering from particular parts of a macromolecular complex. This powerful technique is commonly referred-to as "contrast variation" [11-13].

(iv)   Neutron energies are similar to the energies of atomic and electronic processes, i.e. meV to eV range. This allows for the study of the various dynamic properties (i.e., translations, rotations, vibrations and lattice modes) exhibited by molecules and eV transitions within the electronic structure of materials [14-16].

(v)   Because they possess a magnetic moment (spin 1/2 particles), neutrons are ideally suited to the study of magnetic structures (short- and long-range) and short wavelength magnetic fluctuations. It is important to note that the cross-sections for magnetic scattering are of the same magnitude to those for nuclear scattering [17-18].

SMALL ANGLE NEUTRON SCATTERING (SANS)

Small angle neutron scattering (SANS) probes structure in materials of length scales ranging from tens of angstroms (10^{-9} m) to hundreds of nanometers (10^{-7} m) [19]. The length scale, d, is determined by the neutron wavelength, λ, and the scattering angle, θ, through the relationship

$$\lambda = 2d \sin \theta/2,$$

John Katsaras <john.katsaras@nrc-cnrc.gc.ca>[a,b,c], Thad A. Harroun[c], Jeremy Pencer[a], Thomas Abraham[a], Norbert Kučerka[a], and Mu-Ping Nieh[a]; [a]Canadian Neutron Beam Centre, National Research Council Canada, Chalk River Laboratories, Chalk River, ON, K0J 1J0; [b]Biophysics Interdepartmental Group, Guelph-Waterloo Institute for Physics, Guelph, ON, N1G 2W1; [c]Department of Physics, Brock University, St. Catharines, ON, L2S 3A1

commonly referred-to as Bragg's Law. Through the use of cold (*i.e.* long wavelength) neutrons and the appropriate beam collimation, length scales approaching tens of micrometers are possible [20,21].

In general, SANS can provide information regarding a particle's size and shape, distribution of scattering inhomogeneities, conformational changes and molecular associations in solution. More importantly, because of the properties of neutrons individual components within a macromolecule can be systematically manipulated either through isotopic labelling or the judicious use of solvents. Below we will discuss SANS instrumentation and provide a few examples of SANS data obtained from lipid/water and surfactant/water systems.

SANS INSTRUMENTATION

Figure 1 shows a schematic of a typical SANS instrument located at a neutron source capable of producing long wavelength ($\lambda \sim 5 - 20$ Å) or commonly referred-to, "cold neutrons" [22]. Velocities (*i.e.*, wavelengths) of the incoming neu-
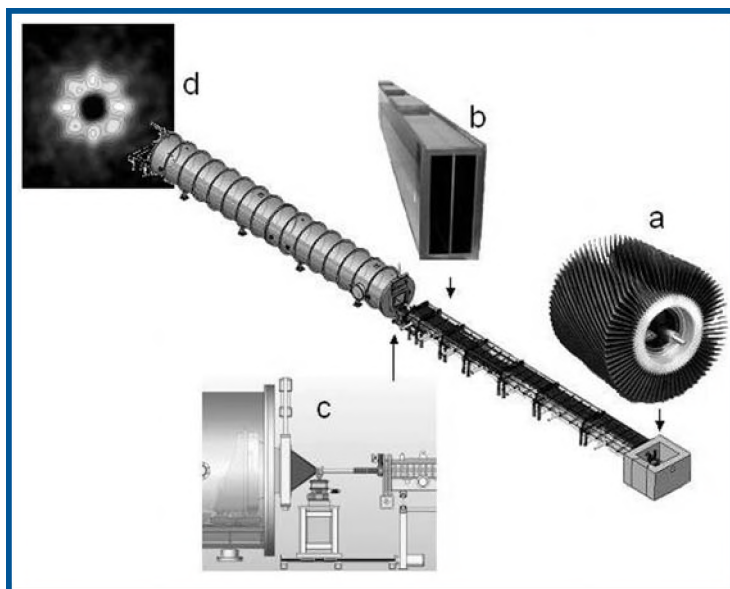
Fig. 1   Schematic of a typical SANS instrument utilizing long wavelength or commonly referred-to cold neutrons. Velocities (i.e., wavelengths) of incoming neutrons are chosen by a mechanical velocity selector (a). For a given cylinder length, L, and a spiral pitch, p, if the cylinder spins on its axis at an angular velocity ω only neutrons of velocity, V (= $p\omega/2\pi$) are transmitted. Reasonably monoenergetic cold neutrons are transported over meters and collimated through a series of nickel-coated or supermirror (e.g., Ni/Ti multilayers) guides (b). The evacuated guides, which transport cold neutrons via total external reflection, are made of optically flat glass and their interiors are coated with either nickel, or its isotope ^{58}Ni (larger critical angle, θ_c, increased $\Delta\lambda/\lambda$), or multilayers of Ni/Ti, which offer an even greater θ_c. Neutrons then interact with the sample (c), which scatters neutrons usually detected by a ^{3}He-filled 2D detector (neutron + ^{3}He → ^{3}H + ^{1}H + 0.76 MeV) (d). The flight path in which the 2D detector is housed is evacuated, resulting in a reduced background.

trons are chosen by a mechanical velocity selector, basically, a high-speed rotor. The helically twisted rotor blades are coated with ^{10}B, a neutron absorbing material, and reasonably monochromatized neutrons (bandpass, $\Delta\lambda/\lambda$ of $\sim 10\%$) are obtained by varying the rotor speed (revolutions/minute, rpm). Those neutrons whose velocities are not synchronized to the rotor speed are absorbed by the ^{10}B coated blades. Monochromatic neutrons are then transported over meters and are collimated through a series of nickel-coated guides, which take advantage of the wave-like properties of neutrons.

The propagation characteristics of neutrons involves the refractive index (n) of the medium. Since the critical angle (θ_c) depends on the refractive indices of the media that the neutrons traverse, when $n_{medium} < n_{air}$ neutrons are transported along the length of the guide by a mechanism known as total external reflection ($\theta_{incident} < \theta_c$). For neutrons $n = 1 - (\lambda^2 p/2\pi)$ and the scattering length density, ρ is equal to $\Sigma b_i/V$, where b_i is the coherent scattering length and V is the sample volume. Neutron guides are made of optically flat glass whose interior is generally coated with nickel or its isotope ^{58}Ni (larger θ_c and increased $\Delta\lambda/\lambda$). Since, for neutrons, the index of refraction of ^{58}Ni is slightly less than one, then all neutrons with an angle $< \theta_c$ (*i.e.*, $< 0.5°$ for $\lambda = 5$ Å neutrons) are transported.

Recently developed supermirrors made up, for example, of Ni/Ti multilayers can increase the effective θ_c by up to a factor of 3, compared to pure Ni [23]. They do so not only by utilizing the total external reflection component, but also the superimposed constructive interference (Bragg reflection) from the successive layers of Ni, effectively extending the plateau of total external reflection. The desired energy neutrons impinge on the sample, which when scattered, are usually detected by a ^{3}He-filled two-dimensional (2D) detector.

SANS INFORMATION AT A GLANCE: FRACTAL DIMENSIONALITY

For objects with a radius of gyration, R_G, and $Q << 1/R_G$ where $Q = 4\pi/\lambda \sin \theta/2$, plotting $\ln[I(Q)]$ vs Q^2 results in a straight line of slope $-R_G^2/3$, commonly referred to as a Guinier plot. However, when $Q >> 1/R_G$ $I(Q)$ decays as $Q^{-\alpha}$, where α is the fractal dimension of the scattering object. In this case, fractal refers to a complex structure made up of geometrical objects (self-similarity). The magnitude of α permits for the geometry (*i.e.* morphology) of the scattering object to be determined. In the case where the Q-range of the scattering data is sufficiently large (over one decade in Q) [24], one can estimate α by simply determining the slope of the line from a log-log plot of I(Q) vs Q. Table I shows the fractal dimensions corresponding to various morphologies adopted by biomolecules and polymeric systems.

SANS can also be used to characterize the stability of biological membranes interacting with additive molecules. Of special interest are pharmacologically important molecules that, in appropriate concentrations help to either stabilize the lipid bilayer or cause it to undergo structural change (*e.g.*, lamellar to hexagonal transition). For example, non-ionic surfactant molecules such as, N-dodecyl-N,N-dimethylamine (DDAO)

destabilize dioleoyl phosphatidylcholine (DOPC) bilayers forming mixed micelles whose shape changes, as a function of increasing DDAO concentration, result in rod-like particles (*e.g.*, tubular or cylindrical micelles) and hard sphere objects (*e.g.*, globular micelles) [25].

MORPHOLOGIES OF "BICELLE" MIXTURE LIPIDS DETERMINED BY SANS

Amphipathic phospholipids are one of the main components of biological membranes. They are composed of hydrophobic fatty acid chains and hydrophilic headgroups (Fig. 2), and along with cholesterol are the primary constituents of cell membranes. In purified forms, lipid/water systems form a variety of interesting structures (*e.g.*, lamellar, cubic and hexagonal phases, micelles, *etc.*) (Fig. 3) which for a number of reasons have been the focus of both experimental [26-32] and theoretical interest [33-38]. Many of these structures exhibit features on length scales ranging from nanometers to microns.

In the recent past there has been a great deal of scientific activity in a system forming bilayered micelles, or commonly referred-to "bicelles" [39-40]. As we shall show below, neutron scattering has proven extremely useful in characterizing these systems. Although bicelles were commonly formed in aqueous solutions of ionic surfactants and alcohols [41-43], for biologists a more pertinent system is where the detergent molecules have been substituted by a short chain phospho-
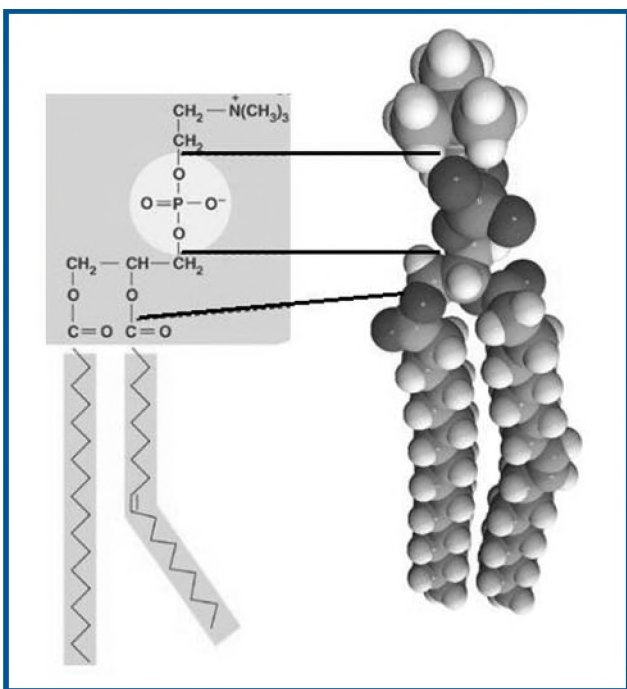
TABLE 1
FRACTAL EXPONENTS FOR VARIOUS MORPHOLOGIES

Rigid Rod	1
Linear Gaussian Chain	2
Chain with Excluded Volume	5/3
Gaussian Chain Randomly Branched	16/7
Swollen Branched Chain	2
Smooth 2D Objects (e.g., lamellar sheets)	2
3D Objects with Smooth Surfaces or Fractal Surfaces (e.g. proteins)	4 3

lipid, such as dihexanoyl phosphatidylcholine (DHPC) [44,45]. In this system, a typical saturated acyl chain lipid, such as dimyristoyl phosphatidylcholine (DMPC, di-14:0 hydrocarbon chains), forms a disk-shaped bilayer whose edges are stabilized by a curved monolayer of detergent [46]. Since their discovery, bilayered micelles have been used in a number of studies attempting to elucidate the structure of proteins under physiologically relevant conditions [39,45,47,48].

However, as we will show, the bilayered micelle morphology is just one of many structures that these lipid mixtures are capable of adopting.

COMPLETE UNBINDING OF LAMELLAE: FORMATION OF UNILAMELLAR VESICLES

Figure 4 shows SANS profiles of varying wt% DMPC/DHPC lipid mixtures doped with the negatively charged lipid, dimyristoyl phosphatidylglycerol (DMPG) [49]. A 25 wt% sample was diluted in single steps, at 45°C, to final wt% concentrations of 18.0, 12.5, 9.0, 5.0, 2.5, 1.25, 0.5, and 0.1. The profiles for lipid concentrations, $c_{lp} \geq$ 2.5 wt% exhibit quasi-Bragg maxima, characteristic of equidistant lamellae (*i.e.*, multibilayers). As a function of increasing amounts of water, the lamellar repeat spacing (d-spacing) varied linearly with changes in c_{lp}^{-1}, from 104 to 1348 Å with the lamellar reflec-
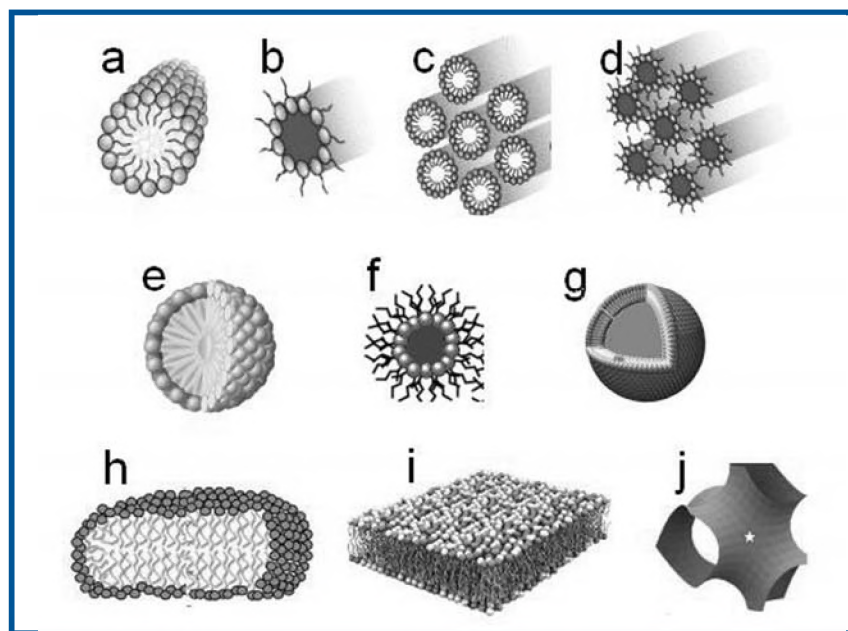

Fig. 2 **Chemical composition and space-filling model of 1-stearoyl-2-oleoyl-*sn*-glycero-3-phosphocholine (18:0-18:1 PC). This lipid is composed of a hydrophilic phosphorylcholine headgroup, a glycerol backbone, and two hydrophobic hydrocarbon chains.**

Fig. 3 **Example morphologies adopted by lipids: (a) Prolate micelle; (b) Inverse prolate micelle; (c) Hexagonal; (d) Inverted hexagonal (e) Micelle; (f) Inverted micelle; (g) Unilamellar vesicle; (h) Bilayered micelle; (e) Bilayer; (j) Cubic.**
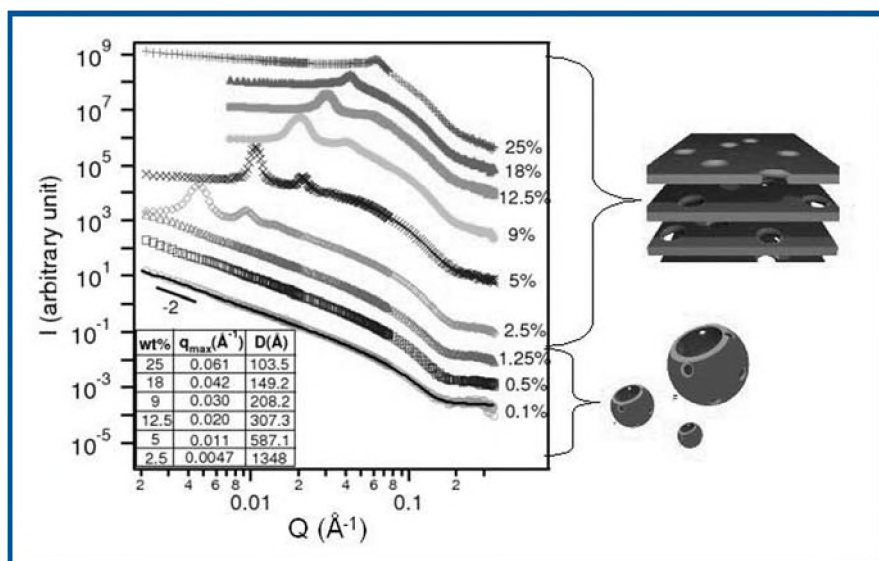
Fig. 4   SANS profiles of (DMPC/DHPC/DMPG) samples prepared and diluted at 45 °C. For all samples, the molar ratios of ([DMPC]+ [DMPG])/[DHPC] and [DMPG]/[DMPC] were fixed at 3.2 and 0.01, respectively. Bragg maxima are evident for 2.5 wt % ≤ c_{lp} ≤ 25 wt % samples, the result of multibilayers with a precise lamellar periodicity, d-spacing. For samples < 2.5 wt %, the multilamellar stacks unbind forming variable size ULV. Note that the SANS profiles decay monotonically and lack the oscillations which are characteristic of monodisperse ULV.
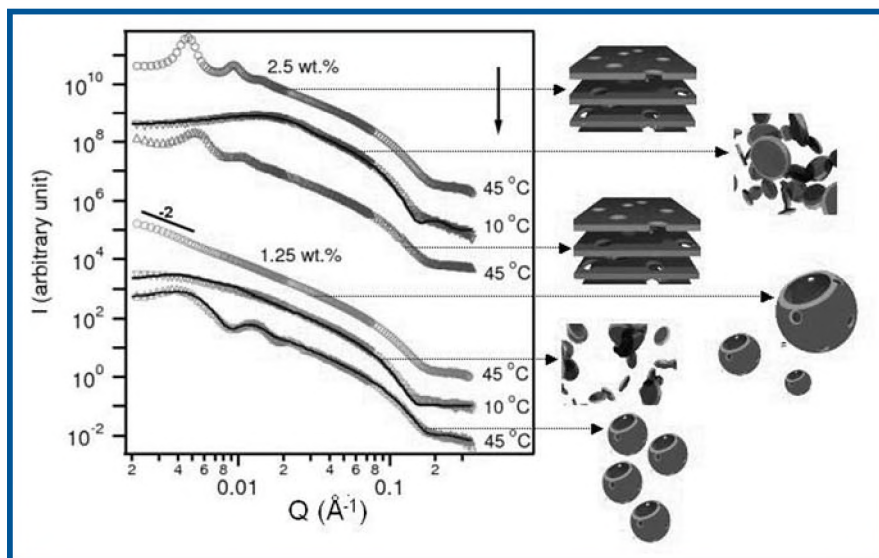
Fig. 5   SANS profiles of 2.5 and 1.25 wt% samples prepared at 45°C (top curve) on cooling to 10°C (middle), and on reheating to 45°C (bottom). The arrow represents the sequence of temperatures. The lamellar phase is recovered in the 2.5 wt % sample, whereas for the 1.25 wt % sample, initially polydisperse ULV become monodisperse on reheating (profile exhibits an oscillatory behaviour as a function of Q). The solid lines are fits to the data.

tions moving systematically to lower values of Q. However, at c_{lp} ≤ 1.25 wt% the lamellar reflections disappear, the result of a complete unbinding transition whereby, the extended lamellar stacks have disintegrated forming variable radii unilamellar vesicles (ULV). The scattered intensity for c_{lp} ≤ 1.25 wt% follows a Q^{-2} dependence over an extended Q

range, representative of isolated bilayers. The data were fit using a model of noninteracting polydisperse ULV.

So what happens if we take some of these morphologies, cool them down to 10°C and reheat back to 45°C? Figure 5 includes SANS data of 1.25 and 2.5 wt% samples. At 10°C the data do not show any sharp peaks and are well described by the bicelle morphology. The data can be best fit to a bilayered disk morphology using a combination of the core-shell-discoidal (CSD) model and the Hayter-Penfold structure factor, $S_{HP}(Q)$, resulting in a disk core radius, R, of 590 and 220 Å for the 1.25 and 2.5 wt% samples, respectively. Not surprisingly, both samples have the same bilayer thickness (42 Å). On reheating to 45°C, the lamellar morphology is recovered in the case of the 2.5 wt% sample. However, of greater interest is that on reheating the 1.25 wt% sample to 45°C, the scattering pattern shows an oscillatory behavior as a function of Q, the fingerprint of monodisperse ULV, instead of the monotonic decay seen initially at 45°C. The data were fit to a ULV model with a $S_{HP}(Q)$ structure factor and a Schulz size distribution yielding an average core radius $<R_i>$ of ~300 Å, a bilayer thickness of 33 Å, and a polydispersity of 0.14. Whereas the ULV were initially large and highly polydisperse (Fig. 5), after temperature cycling they became smaller and more monodisperse. The formation of polydisperse ULV from lamellae is not surprising, since the unbinding of the bilayers does not select any particular length scale. However, the situation is very different when ULV are formed from bicelles, whereby the bilayered micelle morphology dictates the size of ULV formed. Figure 6 pictorially summarizes the various morphologies observed by Nieh et al. [49].

SANS AND CONTRAST VARIATION

For polymeric materials rich in hydrogen, the use of contrast variation and SANS makes for a powerful combination. By judiciously exchanging the molecule's hydrogen atoms for deuteriums, or by changing the solvent's scattering length density (ρ), one can enhance the "visibility" of a molecule's moieties. For example, the optimum contrast conditions for studying the overall bilayer structure are a fully hydrogenated lipid in 100% D_2O solvent. On the other hand a solvent composed of 50:50 D_2O:H_2O provides the best contrast for lipids with perdeuterated chains while the same lipid in a pure D_2O provides information mainly about the lipid's headgroup. The data obtained from these experiments can then be analyzed using either model dependent or model independent methods.

A model independent method based on the Guinier approximation (i.e., low Q region) provides a reasonably straightforward procedure for extracting the bilayer's structural parameters [13]. By analyzing the SANS data obtained at several different contrast conditions, the average bilayer scattering
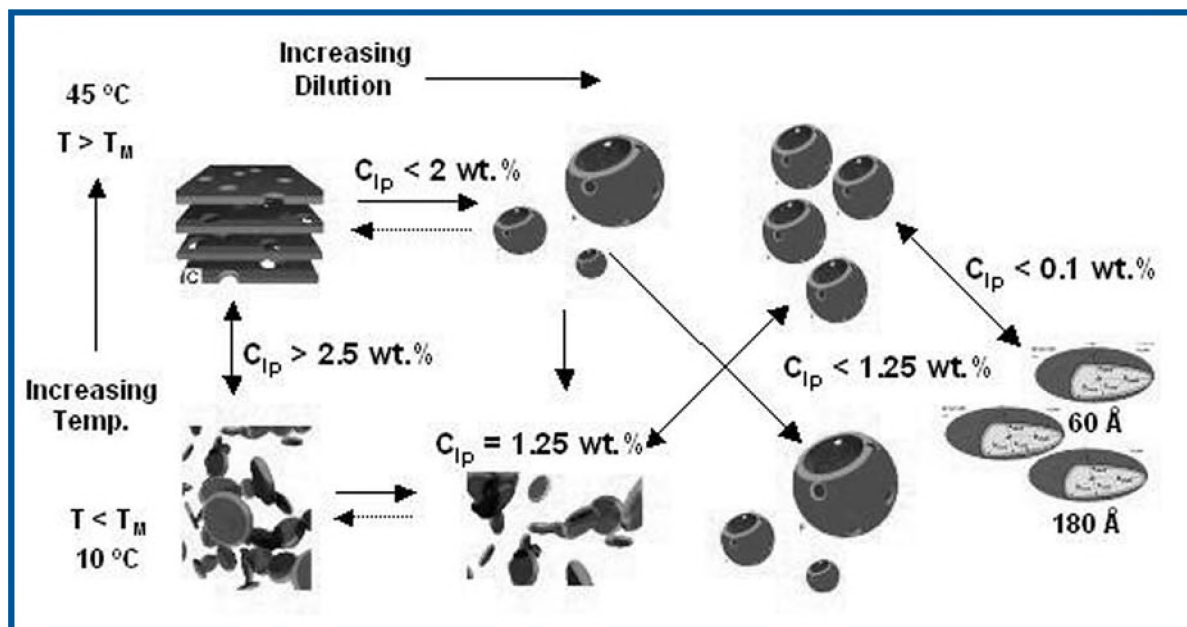
Fig. 6 Schematic summary of the morphological transformations observed by Nieh *et al.*[49]. On diluting below a critical lipid concentration c_{lpu} at $T > T_M$ (chain melting transition of DMPC), extended bilayer sheets unbind into a polydisperse ULV dispersion. On cooling below T_M and $c_{lpu} \geq c_{lp} \geq 1.25$ wt %, polydisperse ULV transform into an isotropic bicellar solution, which on reheating to $T > T_M$, gives rise to monodisperse ULV. For $c_{lp} \leq 0.5$ wt % polydisperse ULV are trapped and cannot, at low T, transform into bicelles. Monodisperse ULV can also be obtained by diluting the bicellar phase below c_{lpu} at $T < T_M$, followed by heating above T_M. In the case of very dilute mixtures, i.e., $c_{lp} \leq 0.1$ wt % and $T < T_M$, bilayered micelles do not reform. Instead, oblate ellipsoids are created. The dashed lines indicate plausible transformations not probed by the experiments carried out by Nieh *et al.*[49].
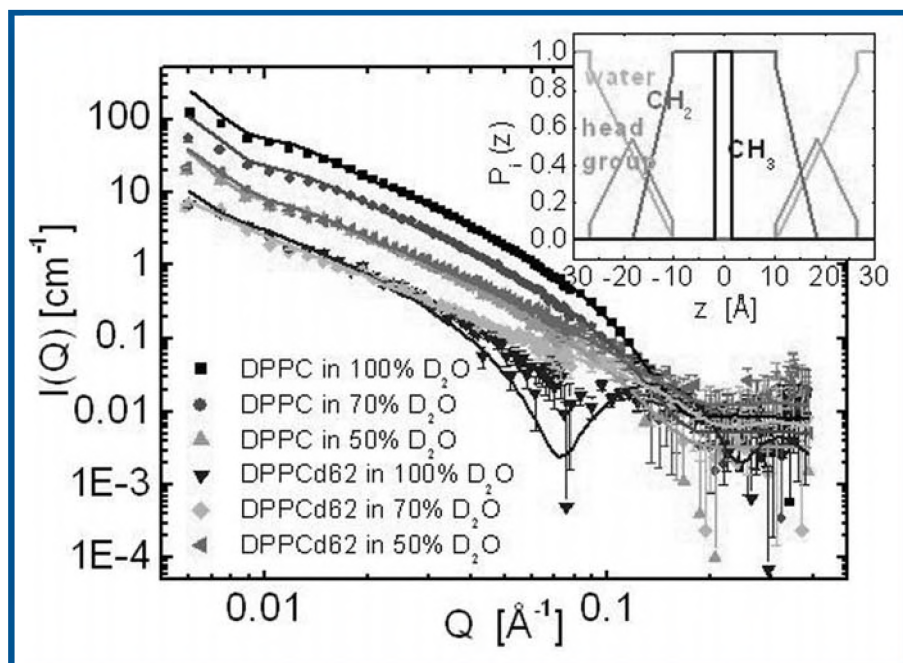
length density is evaluated from the quadratic dependence of the intensity at the origin versus the solvent scattering length density. The radius of gyration (R_G) is evaluated from the slope of the Kratky-Porod plot and then plotted against the inverse of the difference between the solvent and bilayer average scattering length densities. In such a graph, one can obtain R_G at infinitely large contrast corresponding to a point at the graph's origin. Compared to a single SANS measurement, this value - obtained from multiple contrast variation experiments - is a more precise measure of the bilayer's apparent thickness and can be used to study the relative changes in a bilayer using a model-free approach.

Fig. 7 SANS curves obtained at different contrast variation conditions. ULV composed of fully hydrogenated DPPC and DPPC with perdeuterated hydrocarbon chains (d_{62}-DPPC) were prepared in three different $D_2O:H_2O$ (100%, 70% and 50%) mixtures. A molecular model of the bilayer is shown in the inset to the figure. The bilayer profile is represented by probability distribution functions corresponding to solvent molecules, the PC headgroup, and the CH_2 and CH_3 making up the lipid's hydrocarbon chains.

Contrast variation experiments analyzed using a model-based approach enables one to increase the number of independent model parameters leading to more realistic models with better resolved structural features. Scattering curves obtained at different contrast conditions (Fig. 7) are used to capture the different features of the bilayer. A single molecular model of the bilayer is then used to simultaneously fit the different contrast scattering curves. This model is made up of the probability distributions corresponding to the different functional groups (*e.g.*, choline headgroup, hydrocarbon chains, *etc.*) of a bilayer (inset to Fig. 7).

MORPHOLOGY OF GEMINI SURFACTANT AGGREGATES

The aggregation behaviour of Gemini surfactants is another problem that has been examined with SANS. Gemini surfactants are composed of two or more pairs of hydrophilic and hydrophobic groups connected to each other with a spacer (Fig. 8). In order to modify the surface tension of a solution, only small amounts of Gemini surfactants are required as their critical micellar concentration (cmc) in aqueous solutions is much lower than the cmc of conventional surfactants having the same hydrophilic and hydrophobic
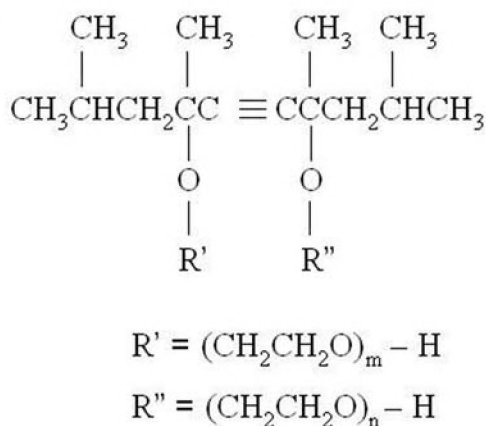
Fig. 8   The molecular structure of α,α'-[2,4,7,9-tetramethyl-5-decyne-4,7-diyl] bis-[ω-hydroxyl-polyoxyethylene].

groups.   One example of what SANS can achieve in studying the structure of such surfactant systems is the molecule α,α'-[2,4,7,9-tetramethyl-5-decyne-4,7-diyl]-bis-[ω-hydroxyl-polyoxyethylene] (Fig. 8), which contains 10 ethylene oxide (EO) segments. Conclusions from previous studies were that the system underwent two possible transitions namely a monomer $\rightarrow$ micelle I and a micelle I $\rightarrow$ micelle II at 0.9 and 2 wt%, respectively [50-53]. However, recent SANS data, outlined below, have contradicted these findings [54].

Figure 9 shows SANS patterns for various surfactant concentrations [54]. At low concentration (0.5 wt%) and a Q-regime of < 0.02 Å^{-1}, I(Q) decays as Q^{-4} decay indicating the presence of large particles (> 50 nm) in solution - denoted later on as "clusters". Between 0.03 and 0.1 Å^{-1} I(Q) plateaus and decays as Q^{-2} for Q > 0.1 Å^{-1}, characteristic of particles with a much smaller length scale, possibly monomer surfactant molecules. As the surfactant concentration increases to 1 wt%, the slope of the scattered intensity decreases at small Q values, indicative of scattering contributions from larger sized "clusters". Moreover, the intensity plateau starts to decay earlier than that seen in the 0.5 wt% sample, implying that the smaller aggregates are getting larger at higher concentrations, presumably due to micellation. The SANS data of the 1 wt% sample also shows a slight upturning at very low Q (< 0.005 Å^{-1}), implying either the coexistence of micelles with small amounts of clusters, or that the size of the clusters, at this concentration, are so large that they are beyond the SANS detecting limit. Above 2 wt% this low Q behaviour disappears completely, indicating that either the clusters have become too large to detect or that they no longer exist.

Analysis of the SANS data can reveal the size and aggregation number of the surfactant. For $Q \cdot R_G \leq 1$ (corresponding to a Q range of 0.01 < Q < 0.04 Å^{-1}) I(Q) can be related to the radius of gyration, R_G, aggregation number, n_s and the second virial coefficient, A_2 (an index for interparticle interaction), as follows
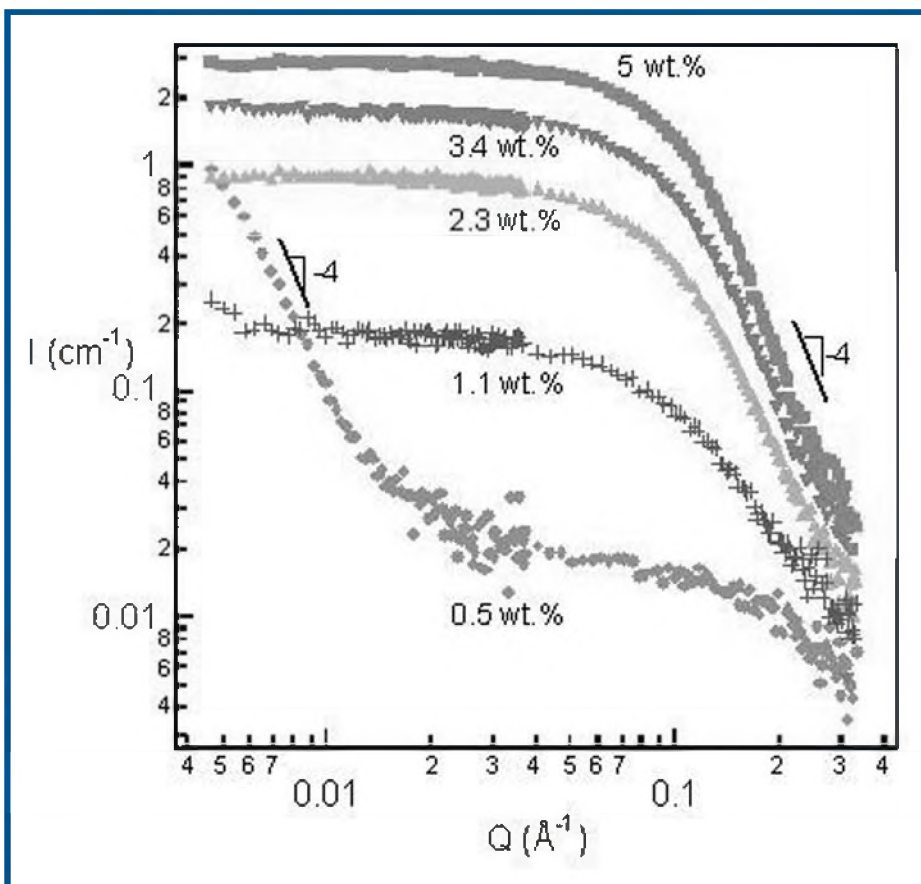

Fig. 9   SANS scattering curves of Gemini surfactants at concentrations varying from 0.5 to 5 wt%.
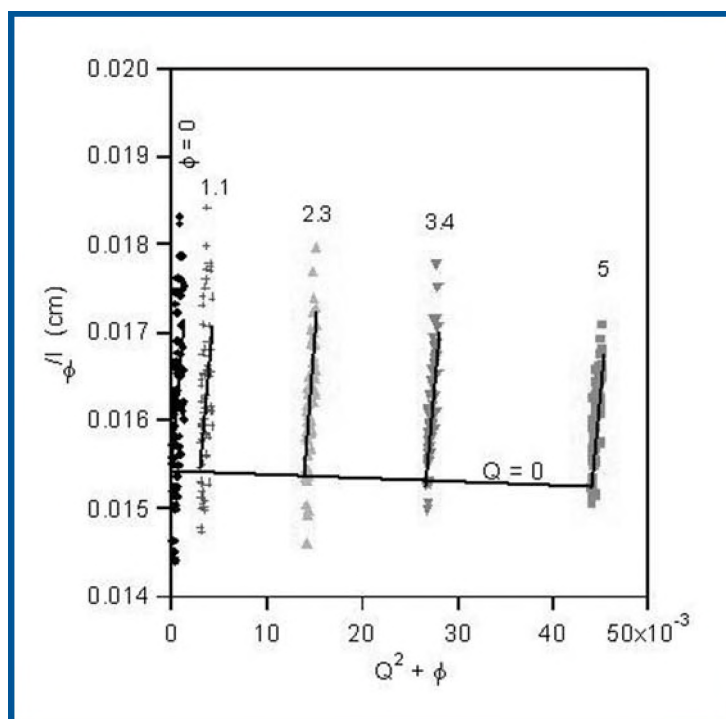

Fig. 10   Zimm plot constructed for SANS data of surfactants with concentrations between 1,1 to 5 wt%. The Q values range from 0.008 to 0.1 Å^{-1}.

$$\frac{\phi}{I(Q)} = \frac{1}{\Delta\rho^2 \left(1 - Q^2 R_G^2 / 3 + \cdots\right)} \left(\frac{1}{v_s n_s} + 2A_2\phi + \cdots\right)$$

$$\sim \frac{\left(1 + Q^2 R_G^2 / 3 + \cdots\right)}{\Delta\rho^2} \left(\frac{1}{v_s n_s} + 2A_2\phi + \cdots\right)$$

where v_s is the volume of one aggregate and $\Delta\rho$ is the difference in scattering length density between the solvent (*i.e.*, D_2O) and the surfactant. This equation is the basis of the Zimm plot. By plotting the extrapolated $\phi=0$ (justifies neglecting intermolecular interferences *i.e.*, structure factor) values from $\phi/I(Q)$ versus Q^2 plots, a straight line is obtained with slope $\dfrac{R_G^3}{3 \cdot v_s n_s \Delta\rho^2}$. On the other hand, by plotting the extrapolated $Q=0$ (justifies the treatment of intramolecular interference *i.e.* form factor) values, a line is obtained with slope $\dfrac{2A_2}{\Delta\rho^2}$. A Zimm plot (Fig. 10) can therefore be constructed with ϕ/I versus $(c\phi+Q^2)$, where c is an arbitrary constant allowing for the various ϕ lines to be separated. The obtained R_G, n_s and A_2 values for micelles are (14.7 ± 3.5) Å, (17.2 ± 0.2), and $(-2 \pm 6) \times 10^{-5}$ mol/cm^3, respectively. From the analysis of the SANS data the two morphological transitions identified were clusters/monomers → clusters/micelles and clusters/micelles → micelles.

CONCLUDING REMARKS

With regards to polymeric materials, SANS is arguably the single most important neutron scattering technique. It is used routinely to probe the size, shape and conformation of macromolecular complexes whose size ranges from ten to one thousand Ångstroms. In the case of biologically relevant materials, SANS is employed to study molecules and molecular assemblies under physiologically meaningful conditions, and also allows for the study of disordered materials that are difficult or impossible to crystallize. It should be pointed out that the use of SANS has flourished in the last decade from the production of cold neutrons (*i.e.*, 5 – 20 Å) whose long wavelengths have greatly facilitated the interrogation of materials with large unit cells (*e.g.* proteins).

REFERENCES:

1. W. Mampe, P. Ageron, C. Bates, J.M. Pendlebury, and A. Steyerl, "Neutron Lifetime Measured with Stored Ultracold Neutrons", *Phys. Rev. Lett.* **63**, 593–596 (1989).
2. S. Arzumanov, L. Bondarenko, S. Chernyavsky, W. Drexel, A. Fomin, P. Geltenbort, V. Morozov, Yu. Panin, J. Pendlebury, and K. Schreckenbach, "Neutron Life Time Value Measured by Storing Ultracold Neutrons with Detection of Inelastically Scattered Neutrons", *Phys. Lett.* **B483**, 15-22 (2000).
3. V.F. Sears, "Neutron Scattering Lengths and Cross Sections", *Neutron News* 3, 226-37 (1992).
4. J.P. Bradshaw, M.J.M. Darkes, T.A. Harroun, J. Katsaras, and R.M. Epand, "Oblique Membrane Insertion of Viral Fusion Peptide Probed by Neutron Diffraction", Biochemistry **39**, 6581- 6585 (2000).
5. T.A Harroun, J. Katsaras, and S.R. Wassall, "Cholesterol Hydroxyl Group is Found to Reside in the Center of a Polyunsaturated Lipid Membrane", *Biochemistry* **45**, 1227-1233 (2006).
6. J. Katsaras, "Highly Aligned Lipid Membrane Systems in the Physiologically Relevant 'Excess water' Condition", *Biophys. J.* **7**, 2924-2929 (1997).
7. J. Katsaras, "Adsorbed to a Rigid Substrate, DMPC Multibilayers Attain Full Hydration in All Mesophases", *Biophys. J.* **75**, 2157-2162 (1998).
8. T.A. Harroun, H. Fritzsche, M.J. Watson, K.G. Yager, O.M. Tanchak, C.J. Barrett, and J. Katsaras, "A Variable Temperature, Relative Humidity (0 - 100% RH), and Liquid Neutron Reflectometry Sample Cell Suitable Cell Suitable for Polymeric and Biomimetic Materials", *Rev. Sci. Insrum.* **76**, 065101(1)-065101(5) (2005).
9. A.J. Berry and M. James, "Refinement of Hydrogen Positions in Synthetic Hydroxyl-Clinohumite by Powder Neutron Diffraction", Amer. Miner. **86**, 181-184 (2001).
10. T. Gutberlet, U. Heinemann, and M. Steiner, "Protein Crystallography with Neutrons – Status and Perspectives", *Acta Cryst.* **D57**, 349-354 (2001).
11. B. Jacrot, "The Study of Biological Structures by Neutron Scattering from Solution", *Rep. Prog. Phys.* **39**, 911-953 (1976).
12. J. Witz, "Contrast Variation of the Small-Angle Neutron Scattering of Globular Particles: The Influence of Hydrogen Exchange", *Acta Cryst.* **A39**, 706-711 (1983).
13. N. Kučerka, D. Uhríková, J. Teixeira, and P. Balgavý, "Bilayer Thickness in Unilamellar Phosphatidylcholine Vesicles: Small-Angle Neutron Scattering Using Contrast Variation", *Physica B* **350**, e639-e642 (2004).
14. S. Cusack and W. Doster, Temperature Dependence of the Low Frequency Dynamics of Myoglobin. Measurement of the Vibrational Frequency Distribution by Inelastic Neutron Scattering", *Biophys. J.* **58**, 243-251 (1990).
15. V. Réat, H. Patzelt, M. Ferrand, C. Pfister, D. Oesterhelt, and G. Zaccai, "Dynamics of Different Functional Parts of Bacteriorhodopsin: H-2H Labeling and Neutron Scattering", *Proc. Natl. Acad. Sci. USA* **95**, 4970-4975 (1998).
16. G. Zaccai, "How Soft is a Protein? A Protein Dynamic Force Constant Measured by Neutron Scattering", *Science* **288**, 1604-1607 (2000).
17. S. Mangin, F. Montaigne, C. Bellouard, and H. Fritzsche, "Study of Magnetic Configurations in Exchange-Coupled Bilayers by Polarized Neutron Reflectometry, *Appl. Phys. A.* **74**, s631-s633 (2004).
18. H. Fritzsche, "Antiferromagnetic Structure of Thin Cr(110) Films in Large Magnetic Fields", *J. Magn. Magn. Mater.* **302**, 160-164 (2006).
19. J.K. Krueger and G.D. Wignall, "Small-Angle Neutron Scattering from Biological Molecules", in *Neutron Scattering in Biology: Techniques and Applications*, J. Fitter, T. Gutberlet, and J. Katsaras (eds), Springer, Germany. p. 27-160, (2006).
20. M. Agamalian, G.D. Wignall, and R. Triolo, "Optimization of a Bonse-Hart Ultra-Small-Angle Neutron Scattering Facility by Elimination of the Rocking-Curve Wings", *J. Appl. Cryst.* **30**, 345-352 (1997).
21. C.D. Muzny, B.D. Butler, H.J.M. Hanley, and M. Agamalian, "An Ultra-Small-Angle Neutron Scattering Study of the Restructuring of Sheared Colloidal Silica Gels", *J. Phys.* **11**, L295-L298 (1999).
22. C.J. Glinka, J.G. Barker, B. Hammouda, S. Krueger, J.J. Moyer, and W.J. Orts, "The 30 m Small-Angle Neutron Scattering Instruments at the National Institute of Standards and Technology", *J. Appl. Cryst.* **31**, 430-445 (1998).
23. Ch. Rehm, and M. Agamalian, "Flux Gain for a Next-Generation Neutron Reflectometer Resulting from Improved Supermirror Performance", *Appl. Phys.* **A74**, S1483–S1485 (2002).
24. J.S. Higgins and H.C. Benoît, "Polymers and Neutron Scattering", *Claredon Press*, Oxford (1996).

25. D. Uhríková, N. Kučerka, A. Islamov, V. Gordeliy and P. Balgavý, "Small-Angle Neutron Study of N-Dodecyl-N,N-dimethylamine N-Oxide Induced Solubilization of Dioleoylphosphatidylcholine Bilayers in Liposomes", *Gen. Physiol. Biophys.* **20**, 183-189 (2001).

26. G.S. Smith, E.B. Sirota, C.R. Safinya, and N.A. Clark, " Structure of the L_A Phases in a Hydrated Phosphatidylcholine Multimembrane", *Phys. Rev. Lett.* **60**, 813-816 (1988).

27. J. Katsaras and R.H. Stinson, "High-Resolution Electron density Profiles Reveal Influence of Fatty Acids on Bilayer Structure", *Biophys. J.* **57**, 649-655 (1990).

28. V.A. Raghunathan and J. Katsaras, "Structure of the $L_{c'}$ Phase in a Hydrated Lipid Multilamellar System", *Phys. Rev. Lett.* **74**, 4456-4459 (1995).

29. J. Katsaras and V.A. Raghunathan, "Evidence for a Two-Dimensional Lattice in Subgel Phase DPPC Bilayers", *Biochemistry* **34**, 4684-4688 (1995).

30. J. Katsaras and V.A. Raghunathan, "Molecular Chirality and the "Ripple" Phase of Phosphatidylcholine Multibilayers", *Phys. Rev. Lett.* **74**, 2022-2025 (1995).

31. B. Pozo-Navas, V.A. Raghunathan, J. Katsaras, M. Rappolt, K. Lohner, and G. Pabst, "Discontinuous Unbinding of Lipid Bilayers", *Phys. Rev. Lett.* **91**, 028101(1)-028101(4) (2003).

32. T.A. Harroun, J. Katsaras, and S.R. Wassall, "Cholesterol Hydroxyl Group is Found to Reside in the Center of a Polyunsaturated Lipid Membrane", *Biochemistry* **45**, 1227-1233 (2006).

33. W. Helfrich, "Elastic Properties of Lipid Bilayers: Theory and Possible Experiments", *Z. Naturforsch.* **28c**, 693-703 (1973).

34. W. Helfrich, "Steric Interaction of Fluid Membranes in Multilayer Systems", *Z. Naturforsch.* **33a**, 305-315 (1978).

35. R. Lipowsky and S. Leibler, "Unbinding Transitions of Interacting Membranes", *Phys. Rev. Lett.* **56**, 2541-2544 (1986).

36. M. Mutz and W. Helfrich, "Bending Rigidities of Some Biological Model Membranes as Obtained from the Fourier Analysis of Contour Sections", *J. Phys. Fr.* **51**, 991-1002 (1990).

37. T.C. Lubensky and F.C. MacKintosh, "Theory of "Ripple" Phases of Lipid Bilayers", *Phys. Rev. Lett.* **71**, 1565-1568 (1993).

38. J.F. Nagle and J. Katsaras, "Absence of a Vestigial Vapor Pressure Paradox", *Phys. Rev.* **E59**, 7018-7024 (1999).

39. C.R. Sanders 2nd and G.C. Landis, "Reconstitution of Membrane Proteins into Lipid-Rich Bilayered Mixed Micelles for NMR-Studies", *Biochemistry* **34**, 4030-4040 (1995).

40. J. Katsaras, R.L. Donaberger, I.P. Swainson, D.C. Tennant, Z. Tun, R.R. Vold, and R.S. Prosser, "Rarely Observed Phase Transitions in a Novel Lyotropic Liquid Crystal System", *Phys. Rev. Lett.* **78**, 899-902 (1997).

41. K.D. Lawson and T.J. Flautt, "Magnetically Oriented Lyotropic Liquid Crystalline Phases", *J. Am. Chem. Soc.* **89**, 5489-5491 (1967).

42. F.Y. Fujiwara and L.W. Reeves, "Mesophase Behavior and Structure of Type I Lyotropic Liquid Crystals", *J. Phys. Chem.* **84**, 653-661 (1980).

43. B.J. Forrest and L.W. Reeves, "New Lyotropic Liquid Crystals Composed of Finite Nonspherical Micelles. *Chem. Rev.* **81**, 1-14 (1981).

44. C.R. Sanders 2nd and J.P. Schwonek, "Characterization of Magnetically Orientable Bilayers in Mixtures of Dihexanoylphosphatidylcholine and Dimyristoylphosphatidylcholine by Solid-State NMR", *Biochemistry* **31**, 8898-8905 (1992).

45. C.R. Sanders, B.J. Hare, K. Howard and J.H. Prestegard, "Magnetically Oriented Phospholipid Micelles as a Tool for the Study of Membrane-Associated Molecules", *Prog. NMR Spect.* **26**, 421-444 (1994).

46. C.R. Sanders 2nd and J.H. Prestegard, "Magnetically Orientable Phospholipid Bilayers Containing Small Amounts of Bile Salt Analogue, CHAPSO", *Biophys. J.* **58**, 447-460 (1990).

47. N. Tjandra and A. Bax, "Direct Measurement of Distances and Angles in Biomolecules by NMR in a Dilute Liquid Crystalline Medium", *Science* **278**, 1111-1114 (1997).

48. J. Struppe, J.A. Whiles, and R.R. Vold, "Acidic Phospholipid Bicelles: A Versatile Model Membrane System", *Biophys. J.* **78**, 281-289 (2000).

49. M.-P. Nieh, V.A. Raghunathan, S.R. Kline, T.A. Harroun, C.-Y. Huang, J. Pencer, and J. Katsaras, "Spontaneously Formed Unilamellar Vesicles with Pat-Dependent Size Distribution", *Langmuir* **21**, 6656-6661 (2005).

50. S. Sato, H. Kishimoto, "Thermodynamic And Viscometric Studies on the Solution State of Surfynol 465 in Water", *Bull. Chem. Soc. Jnp.* **58**, 282-287 (1985).

51. S. Sato, H. Kishimoto, "Enthalpic Studies on the Formation And Interaction of Micelles of A Nonionic, Surfynol 465", *J. Colloid Interface Sci.* **123**, 216-223 (1988).

52. S. Sato, H. Kishimoto, "Osmotic And Activity Coefficients of A Nonionic, Surfynol 465 as Its Higher Concentrations in Water", *J. Colloid Interface Sci.* **126**, 108-113 (1988).

53. S. Sato, "Micellar Behavior of A Nonionic Surfactant, Surfynol 465, from Carbon-13 NMR Resonance Frequencies in D_2O", *J. Phys. Chem.* **93**, 4829-4833 (1989).

54. M.-P. Nieh, S. Kumar, R.H. Fernando, R. Colby, J. Katsaras, "Effect of the Hydrophilic Size on the Structural Phases of Aqueous Nonionic Gemini Surfactant Solutions", *Langmuir* **20**, 9061-9068 (2004).